




Cite this: *Nanoscale*, 2019, **11**, 23217

An Fe stabilized metallic phase of NiS₂ for the highly efficient oxygen evolution reaction†

Xingyu Ding,^a Weiwei Li,^b Haipeng Kuang,^a Mei Qu,^a Meiyang Cui,^a Chenhao Zhao,^a Dong-Chen Qi,^c Freddy E. Oropeza^{*d} and Kelvin H. L. Zhang ^{*a}

This work reports a fundamental study on the relationship of the electronic structure, catalytic activity and surface reconstruction process of Fe doped NiS₂ (Fe_xNi_{1-x}S₂) for the oxygen evolution reaction (OER). A combined photoemission and X-ray absorption spectroscopic study reveals that Fe doping introduces more occupied Fe 3d⁶ states at the top of the valence band and thereby induces a metallic phase. Meanwhile, Fe doping also significantly increases the OER activity and results in much better stability with the optimum found for Fe_{0.1}Ni_{0.9}S₂. More importantly, we performed detailed characterization to track the evolution of the structure and composition of the catalysts after different cycles of OER testing. Our results further confirmed that the catalysts gradually transform into amorphous (oxy)hydroxides which are the actual active species for the OER. However, a fast phase transformation in NiS₂ is accompanied by a decrease of OER activity, because of the formation of a thick insulating NiOOH layer limiting electron transfer. On the other hand, Fe doping retards the process of transformation, because of a shorter Fe–S bond length (2.259 Å) than Ni–S (2.400 Å), explaining the better electrochemical stability of Fe_{0.1}Ni_{0.9}S₂. These results suggest that the formation of a thin surface layer of NiFe (oxy)hydroxide as an active OER catalyst and the remaining Fe_{0.1}Ni_{0.9}S₂ as a conductive core for fast electron transfer is the base for the high OER activity of Fe_xNi_{1-x}S₂. Our work provides important insight and design principle for metal chalcogenides as highly active OER catalysts.

Received 11th September 2019,
Accepted 4th November 2019

DOI: 10.1039/c9nr07832k

rsc.li/nanoscale

1. Introduction

Electrolysis of water to produce H₂ and O₂ is a promising pathway for storage of solar or other renewable energies in the form of chemical fuels.¹ However, the overall efficiency is limited by the sluggish kinetics of the oxygen evolution reaction (OER) that involves a thermodynamically uphill and complex four-electron/proton transfer process.² Hence, an efficient and low-cost OER electrocatalyst becomes the key to improve the efficiency. Over the past few years, a variety of transition metal (TM)-based electrocatalysts, including oxides,^{3–6} chalcogenides,^{7,8} nitrides,^{9,10} and phosphides,^{11,12}

have been explored as OER electrocatalysts. TM oxides are the mostly studied material system. Similar to the d-band center theory established for noble metal catalysis, the OER activity is generally governed by the adsorption binding strength of reaction intermediates on catalyst surfaces, where optimal performance is achieved when the reaction intermediates bind neither too strongly nor too weakly.¹³ The optimal adsorption strength for the high performance OER has been correlated with various electronic parameters of TM oxides, such as the number of electrons in the e_g orbitals of TM cations (with e_g = 1.2 showing the best OER performance),¹⁴ covalency of 3d–O 2p,¹⁵ energy position of the O 2p band center¹⁶ and lattice oxygen.¹⁷ This knowledge provides essential guidelines to achieve highly active electrocatalysts by tailoring these electronic parameters through doping,^{18–21} strain^{22–24} and creation of oxygen defects.²⁵

On the other hand, recently TM chalcogenides, nitrides and phosphides have been shown to exhibit not only higher OER activity than oxides,^{26,27} but also superior activity toward the hydrogen evolution reaction (HER).^{28–31} One advantage of these materials over oxides is that they usually show metallic conductivity because of more hybridization between TM 3d and anion p orbitals (e.g., S 3p and Se 4p).^{32–34} Among these materials, nickel sulfides (NiS₂, NiS and Ni₃S₂) have attracted extensive attention.^{35,36} Key strategies to improve the activity

^aState Key Laboratory of Physical Chemistry of Solid Surfaces, College of Chemistry and Chemical Engineering, Xiamen University, Xiamen 361005, P.R. China.

E-mail: kelvinzhang@xmu.edu.cn

^bDepartment of Materials Science & Metallurgy, University of Cambridge, 27 Charles Babbage Road, Cambridge, CB3 0FS, UK

^cSchool of Chemistry, Physics and Mechanical Engineering, Queensland University of Technology, Brisbane, Queensland 4001, Australia

^dLaboratory of Inorganic Materials Chemistry, Department of Chemical Engineering and Chemistry, Eindhoven University of Technology, P. O. Box 513, 5600MB Eindhoven, The Netherlands. E-mail: freddyorozeza@gmail.com

†Electronic supplementary information (ESI) available. See DOI: 10.1039/c9nr07832k

include nanostructuring to increase the surface area and doping or creating defects to improve the intrinsic activity. For example, Liu *et al.* reported that 10% V doping can induce a semiconductor to metal transition in NiS₂ nanosheets.³⁷ The metallic V doped NiS₂ exhibits extraordinary OER electrocatalytic performance with an overpotential of 290 mV at 10 mA cm⁻², because of enhanced conductivity for fast electron transfer during the OER. Furthermore, Yan *et al.* found that Fe³⁺ doping into the surface lattice of the NiS₂ (002) facet can modulate the electronic structure of active centers, and lower the activation energy for the HER.³⁸ A similar doping strategy was also applied to other material systems such as Ni-based oxides,³⁹ Ni₃S₂,⁴⁰ NiSe⁴¹ and Ni₂P.⁴² These reports agreed in that modulation of electronic structures, *e.g.* an increase of electronic conductivity, can improve the activities for the OER and HER. However, there are limited studies elucidating how the electronic structures are modulated by doping. Furthermore, it has been recognized that TM chalcogenides, nitrides and phosphides tend to transform into their corresponding (oxy)hydroxides at least near the surface region of the catalysts due to the strongly oxidizing conditions of the OER. The transformed TM (oxy)hydroxides are the actual active phase for the OER.^{43–45} However, interestingly, the transformed TM (oxy)hydroxides show much better OER activity than TM (oxy)hydroxides synthesized directly. The origin of this enhanced activity is an important question to address, since it could provide a basis for rational design of high-performance electrodes.

In this work, we address these questions by combining detailed electrochemical characterization with experimental determination of the electronic structure of NiS₂. We synthesized Fe doped NiS₂ (Fe_xNi_{1-x}S₂ with $x = 0, 0.05, 0.10, 0.15$ and 0.20) by sulfidation of FeNi layered double hydroxide (LDH) nanosheets. The evolution of the electronic structure of Fe_xNi_{1-x}S₂ with x was investigated by high-resolution X-ray photoelectron spectroscopy (XPS) and X-ray absorption spectroscopy (XAS). The valence band spectra of Fe_xNi_{1-x}S₂ suggest that Fe doping introduces Fe 3d states near the Fermi level, thus improving electronic conductivity. Meanwhile, Fe doping significantly increases the OER activity of Fe_xNi_{1-x}S₂ with the optimum found for Fe_{0.1}Ni_{0.9}S₂, exhibiting an overpotential of 260 mV at 10 mA cm⁻² and much better stability in 1 M KOH solution. Detailed characterization after different cycles of CV measurement for the OER reveal that the surface of Fe_xNi_{1-x}S₂ is gradually converted to NiFe (oxy) hydroxide which is the actual active phase that promotes the OER, whereas the crystalline pyrite core acts as a conductive channel for electron transfer during the OER. It was found that Fe doping retards the process of transformation because of a stronger Fe–S bond than Ni–S, explaining the much better electrochemical stability and activity of Fe_{0.1}Ni_{0.9}S₂.

2. Experimental section

2.1. Synthesis of Ni and FeNi based layered hydroxides

Fe_xNi_{1-x} LDH nanosheets were synthesized by a one-step hydrothermal method.³⁹ Ferric nitrate (Fe(NO₃)₃) and nickel

chloride (NiCl₂) were used as precursors. Fe_xNi_{1-x} LDH with different x values was prepared by mixing Fe(NO₃)₃ with NiCl₂ with an appropriate molar ratio in a beaker with 72.4 mL deionized (DI) water. 5.6 mL 0.5 M urea aqueous solution and 2 mL 0.01 M trisodium citrate (TSC) aqueous solution were added into the beaker in sequence with magnetic stirring. The mixed solution was transferred into a 100 mL Teflon lined stainless steel autoclave for hydrothermal reaction at 150 °C for 24 hours and cooled to room temperature naturally. The precipitate products were collected by centrifugation, washed with DI water three times and finally dried at 60 °C for 12 hours in a vacuum.

2.2. Synthesis of Fe_xNi_{1-x}S₂ nanosheets

The Fe_xNi_{1-x}S₂ nanosheets were synthesized following similar procedures reported by Liu *et al.*³⁷ Briefly, 1 g sulfur was placed at the farthest upstream position and 0.05 g as-synthesized Fe_xNi_{1-x} LDH nanosheets ($x = 0, 0.05, 0.10, 0.15$ and 0.20) were placed at the downstream position. The sulfurization process was continued for 2 hours under an argon atmosphere at a temperature of 200 °C at the upstream position and 300 °C at the downstream position.

2.3. Materials characterization

The crystal structure was characterized by X-ray diffraction (XRD) with Cu K α radiation. Surface morphology was examined by using a ZEISS Sigma field emission scanning electron microscope (SEM). For transmission electron microscopy (TEM) measurements, samples were dispersed in absolute ethanol solution and then dropped on a Cu grid. A monochromatic Al K α X-ray source ($h\nu = 1486.6$ eV) equipped with a SPECS PHOIBOS 150 electron energy analyzer was used for high-resolution XPS measurements. The total energy resolution was 0.50 eV. The binding energy (BE) was calibrated using polycrystalline Au foil in direct contact with the samples. The samples were loaded in the XPS chambers without any further treatment. The valence band (VB) spectra were collected in the binding energy range of -2 – 12 eV at normal emission. XAS measurements were performed at the soft X-ray spectroscopy beamline of the Australian Synchrotron. The concentration of Fe in Fe_xNi_{1-x}S₂ was measured by inductively coupled plasma mass spectrometry (ICP-MS) measurement.

2.4. Electrochemical measurements

All electrochemical measurements were performed using a three-electrode system controlled by using an electrochemical workstation (CHI 750E) connected with a glassy carbon rotating disk electrode (RDE) configuration (Pine Research Instrumentation). For OER tests, Hg/HgO (1 M KOH) was used as the reference electrode, and a graphite rod was used as the counter electrode. It has been shown that a small trace amount of Fe impurities in the electrolyte can significantly enhance the OER activity of Ni-based materials.⁴⁶ In order to exclude the interference of Fe impurities, we purified the KOH electrolyte using the following purification method. Firstly, 1 g Ni(NO₃)₂·6H₂O (purity, >99.999%) and 4 mL DI water were

added in a H₂SO₄-cleaned polypropylene centrifuge tube. After dissolution, 20 mL 1 M KOH was added. The mixture was shaken and centrifuged to obtain high-purity Ni(OH)₂. The high-purity Ni(OH)₂ was washed three times using 1 M KOH. Then 25 mL 1 M KOH were added to the tube for purification. This mixture was shaken for 15 minutes for re-dispersion, followed by resting for 8 hours. Finally, the purified KOH supernatant was filtered using a filter tip (0.2 μm) and stored in a H₂SO₄-cleaned polypropylene bottle for the following electrochemical measurements.

1 M KOH electrolyte was purged with a flow of O₂ (purity, 99.9%) to ensure its continuous O₂ saturation. To prepare the working electrode, 2.5 mg Fe_xNi_{1-x}S₂ samples and 25 μL 5% Nafion solution were put in a 2 mL mixture of water/isopropanol with a volume ratio of 3:1 and ultrasonicated for 60 minutes to form a homogeneous ink. 40 μL catalyst ink was dropped onto a glassy carbon electrode (GCE) with a diameter of 5 mm and dried in air to form a mass loading of 0.25 mg cm⁻². Cyclic voltammetry (CV) tests were carried out at a scan rate of 50 mV s⁻¹. Linear sweep voltammetry (LSV) polarization curves were acquired at a scan rate of 5 mV s⁻¹ in the potential range from 0.1 to 0.8 V (vs. Hg/HgO). Electrochemical impedance spectroscopy (EIS) was performed at 1.63 V (vs. RHE) in the frequency range of 100 kHz to 1 Hz. Electrochemical active surface area (ECSA) was determined from capacitance measurements in the potential region of no faradaic process at different scan rates of 10, 20, 40, 60, 80, 100, 120 and 200 mV s⁻¹. The potentials were converted to the reversible

hydrogen electrode (RHE) using $E_{\text{RHE}} = E_{\text{Hg/HgO}} + 0.059 \text{ pH} + 0.098 \text{ V}$.

3. Results and discussion

3.1. Structure and electronic structure

The Fe_xNi_{1-x}S₂ ($x = 0, 0.05, 0.10, 0.15$ and 0.20) nanosheets were synthesized *via* gas-phase sulfidation of layered nickel iron hydroxide (details in the Experimental section). Both NiS₂ and FeS₂ adopt cubic pyrite structures with lattice parameters of $a_{\text{NiS}_2} = 5.687 \text{ \AA}$ and $a_{\text{FeS}_2} = 5.405 \text{ \AA}$, which favors the formation of solid solutions. The XRD patterns shown in Fig. 1a confirm that all Fe_xNi_{1-x}S₂ have a single pyrite phase (PDF#88-1709). A shift of diffraction peaks toward higher 2θ angles with increasing Fe content was observed. Fig. 1b summarizes the change of lattice parameters with Fe content. The systematic decrease of lattice parameters is attributed to the shortened Fe-S bond length, and suggests the success of doping Fe at the Ni lattice site. ICP-MS was performed, confirming that the actual x values in Fe_xNi_{1-x}S₂ are in agreement with the intended doping concentrations (Fig. 1c and Table S1†). Moreover, the surface morphology and atomic structure were further studied by SEM and TEM. The SEM images in Fig. 1d show that the as-synthesized Fe_xNi_{1-x}S₂ samples have a sheet-like morphology with a size of a few hundred nm and a thickness of ~20 nm. The large-area TEM image in Fig. 1e indicates that the sheet structure is com-

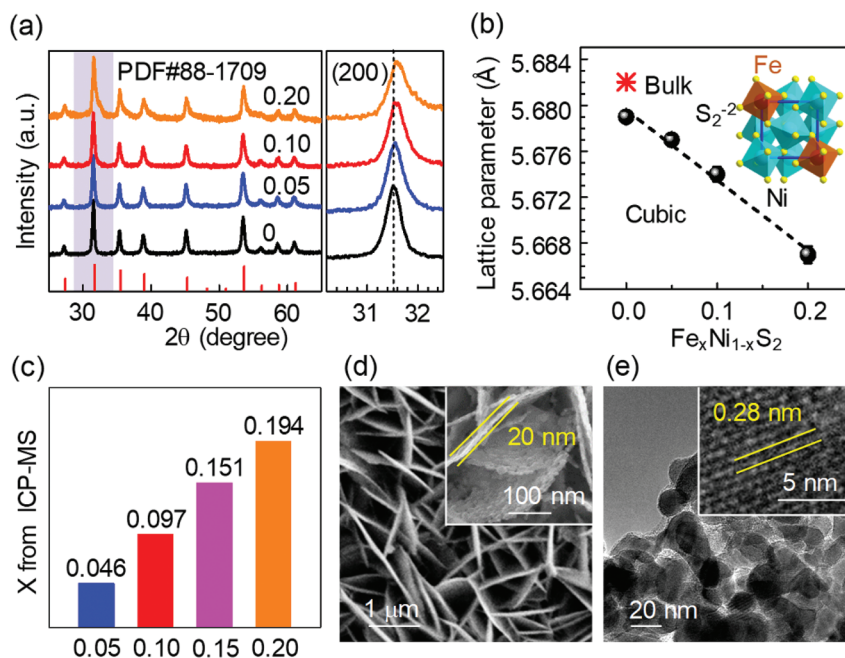


Fig. 1 (a) XRD patterns of Fe_xNi_{1-x}S₂ ($x = 0, 0.05, 0.10$ and 0.20) nanosheets; the right panel shows the zoom-in region around the (200) reflection peak, showing a systematic shift of the peak toward higher 2θ angles with increasing Fe content. (b) Lattice parameters extracted from XRD patterns as a function of x ; the inset shows the schematic crystal structure of pyrite Fe_xNi_{1-x}S₂. (c) Fe contents in Fe_xNi_{1-x}S₂ determined from ICP-MS. (d) SEM image of the as-synthesized Fe_{0.1}Ni_{0.9}S₂ nanosheets; the inset shows a magnified image. (e) TEM image of the as-synthesized Fe_{0.1}Ni_{0.9}S₂ nanosheets; the inset shows a magnified image.

posed of several nano-size sheets with different crystalline domains. The high-resolution TEM image (inset) shows an interplanar spacing of 0.28 nm which matches well with pyrite NiS_2 .

A comprehensive combination of high-resolution XPS and XAS spectra was used to study the effect of Fe doping on the chemical states and electronic structure of $\text{Fe}_x\text{Ni}_{1-x}\text{S}_2$. Fig. 2a shows the Ni 2p XPS spectra for NiS_2 and $x = 0.10$. The Ni 2p spectra show two peaks at binding energies (BEs) of 854.0 eV and 871.4 eV, corresponding to the spin-orbit doublet of Ni $2p_{3/2}$ and $2p_{1/2}$. The BEs and line shapes of Ni 2p and S 2p (Fig. S1†) are in agreement with those for NiS_2 .³⁴ Fe doping does not induce significant changes in the Ni 2p and S 2p spectra. Furthermore, a comparison of Fe 2p spectra with those of FeS_2 and Fe_2O_3 (Fig. 2b) suggests doped Fe is in the +2 oxidation state. The +2 state of Ni and Fe in $\text{Fe}_x\text{Ni}_{1-x}\text{S}_2$ is further confirmed using Ni L-edge and Fe L-edge XAS spectra as shown in Fig. S2.†

XPS VB and S K-edge XAS spectra were used to examine the effect of Fe doping on the electronic structures of NiS_2 . XPS VB measures the occupied density of states (DOS) weighted by the cross-sections of contributing orbitals. S K-edge XAS measures the transition from the S 1s core level to unoccupied states and can be qualitatively related to unoccupied DOS. In the pyrite structure of NiS_2 , each Ni^{2+} cation is octahedrally coordinated by six S_2^{2-} , which split the Ni $3d^8$ into a lower energy t_{2g} state fully occupied by six electrons and a higher energy e_g state occupied by two electrons⁴⁷ (inset in Fig. 2d). Despite the half-filled e_g states, NiS_2 is semiconducting with a bandgap of 0.3 eV due to electron correlations in Ni $3d$.⁴⁸ As shown in Fig. 2c, the XPS VB spectrum of NiS_2 (left panel) con-

sists of four features marked as A–D. Based on the above-mentioned electronic configuration and previous literature,⁴⁹ features A and B are attributed to Ni e_g and t_{2g} states with certain hybridization with S $3p$, whereas C and D are mainly S $3p^6$ states hybridized with Ni $3d$. On the other hand, feature E in S K-edge XAS is assigned to the unoccupied Ni e_g state hybridized with S $3p$.⁵⁰ Fe doping does not induce significant changes in the line shapes of the VB and S K-edge, except that the intensity of feature A increases with increasing the Fe doping level. Because the doped Fe is in $3d^6$ low spin configuration,^{47,50} the increase of feature A originates from the six electron occupied Fe t_{2g} states (inset of Fig. 2d and e). Fig. 2d plots the peak area of feature A as a function of Fe doping. The increased intensity of feature A, *i.e.* density of states near the Fermi level (E_F), suggests improved electronic conductivity with Fe doping. As seen from the direct comparison of the VB and S K-edge spectra of NiS_2 and $\text{Fe}_{0.1}\text{Ni}_{0.9}\text{S}_2$ shown in Fig. 2e, there is a certain amount of DOS across the E_F for $\text{Fe}_{0.1}\text{Ni}_{0.9}\text{S}_2$, indicating a metallic state induced by Fe doping.

3.2. OER performance and mechanism

The OER activities of $\text{Fe}_x\text{Ni}_{1-x}\text{S}_2$ were investigated by comparative sweep voltammetry in O_2 -saturated 1.0 M iron-free KOH. The electrochemical data with 80% iR correction are shown in Fig. 3a. NiS_2 exhibits a high OER overpotential of 380 mV to achieve a current density of 10 mA cm^{-2} , which is in agreement with previous results for pure NiS_2 .⁵¹ Fe doping significantly enhances the OER activity, with optimum performance at $x = 0.10$. As summarized in Fig. 3b, the $\text{Fe}_{0.1}\text{Ni}_{0.9}\text{S}_2$ electrode only requires a low overpotential of 260 mV to achieve a

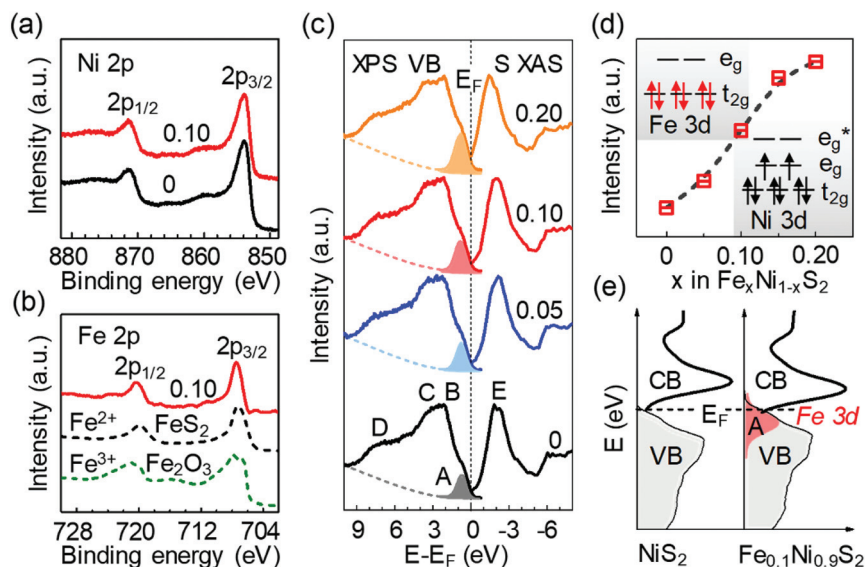


Fig. 2 (a) Ni 2p XPS spectra for the NiS_2 and $\text{Fe}_{0.1}\text{Ni}_{0.9}\text{S}_2$. (b) Fe 2p XPS spectra for $\text{Fe}_{0.1}\text{Ni}_{0.9}\text{S}_2$, and FeS_2 and Fe_2O_3 as references, suggesting that Fe and Ni are in the +2 oxidation state. (c) The XPS valence band (VB) spectra (left) and S K-edge XAS spectra (right) of $\text{Fe}_x\text{Ni}_{1-x}\text{S}_2$ ($x = 0, 0.05, 0.10$ and 0.20). (d) Intensity of peak A marked in (c) as a function of x . The inset shows the schematic electronic configuration of Fe^{2+} and Ni^{2+} in pyrite FeS_2 and NiS_2 . (e) Schematic diagram of electronic structures of NiS_2 and $\text{Fe}_{0.1}\text{Ni}_{0.9}\text{S}_2$. The results suggest that Fe doping introduces Fe $3d$ states near the Fermi level, thus improving the electronic conductivity.

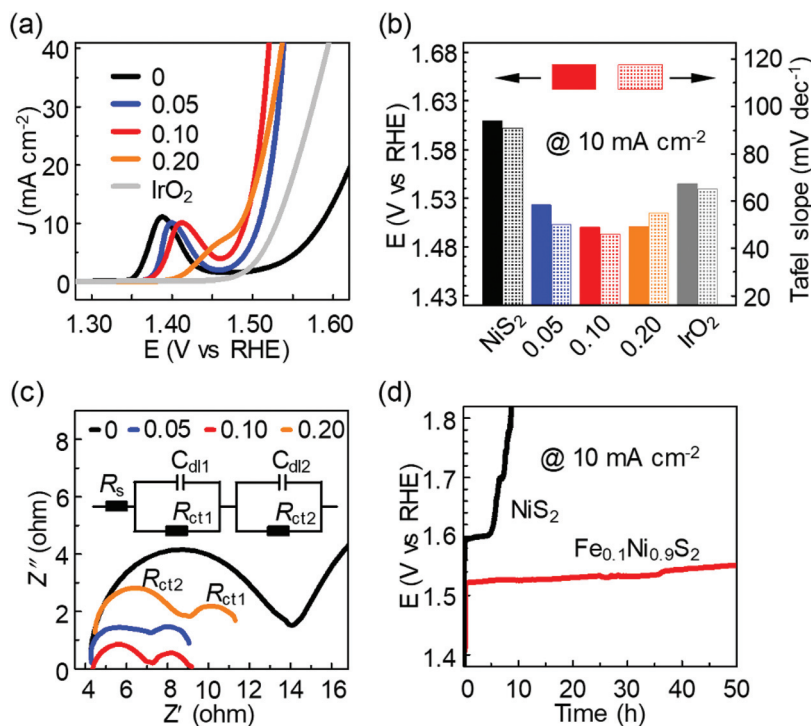


Fig. 3 (a) Linear sweep voltammetry (LSV) polarization curves of $\text{Fe}_x\text{Ni}_{1-x}\text{S}_2$ ($x = 0, 0.05, 0.10$ and 0.20) and IrO_2 measured in 1 M KOH solution. (b) Comparison of potentials for driving 10 mA cm^{-2} current density and Tafel slopes. (c) Nyquist plots of EIS measurements at 1.63 V (vs. RHE) in a sweep frequency range of 100 kHz to 1 Hz. The inset shows the equivalent circuit for fitting the data, consisting of an electrolyte resistance (R_s), a charge transfer resistance (R_{ct1}) caused by electron transfer from the electrolyte to the catalyst, and a resistance (R_{ct2}) caused by electron transfer from the $\text{Fe}_x\text{Ni}_{1-x}\text{OOH}$ layer to the $\text{Fe}_x\text{Ni}_{1-x}\text{S}_2$ layer. (d) Chronopotentiometric curves of NiS_2 and $\text{Fe}_{0.1}\text{Ni}_{0.9}\text{S}_2$ measured under a constant current density of 10 mA cm^{-2} .

current density of 10 mA cm^{-2} . Furthermore, the Tafel slope for NiS_2 is 91 mV dec^{-1} , and is reduced to 50 mV dec^{-1} for $x = 0.05$ and 46 mV dec^{-1} for $x = 0.10$. The significant reduction of the Tafel slope indicates that Fe doping optimizes the reaction energetics for the OER due to the modulation of the electronic structure. Because all samples have a similar morphology (Fig. S3a†) and roughly the same ECSA (Fig. S3b†), the improved OER performance of Fe doped NiS_2 should result from improved intrinsic activity, not from the variation of the surface area. EIS measurements were performed to study the kinetics of charge transfer at the electrode/electrolyte interface (Fig. 3c). $\text{Fe}_{0.1}\text{Ni}_{0.9}\text{S}_2$ displays the smallest Nyquist semicircle, suggesting the lowest charge transfer resistance ($R_{ct1} + R_{ct2}$) for faster electron transfer during the OER process. Fig. 3d shows the chronopotentiometric stability test of NiS_2 and $\text{Fe}_{0.1}\text{Ni}_{0.9}\text{S}_2$, indicating that Fe doping also significantly increases the electrochemical stability of the NiS_2 catalysts. Meanwhile, we can see from Fig. S5† that the performance of NiS_2 degrades rapidly after 5 hours. This is likely caused by the peeling-off/dissociation of NiS_2 .

It has been reported that many TM chalcogenides, nitrides and phosphides tend to transform into their corresponding TM oxides/hydroxides due to the highly oxidizing OER conditions. The TM oxides/hydroxides are the actual active phase for the OER.⁴³ The trend of increased OER activity by Fe

doping in NiS_2 seems to be in accordance with the case of substantially enhanced activity by Fe doping in Ni hydroxides.^{46,52} However, it remains unclear how the phase transformation proceeds during the OER and how it correlates with catalytic activity. To address this question, we performed a comparative study of the transformation process of NiS_2 and $\text{Ni}_{0.1}\text{Fe}_{0.9}\text{S}_2$ after different cycles of OER measurements. For this purpose, we deposited the NiS_2 and $\text{Ni}_{0.1}\text{Fe}_{0.9}\text{S}_2$ on carbon paper, because carbon paper provides supporting substrates for XRD, XPS and XAS measurements after different cycles of CV measurements. The NiS_2 and $\text{Ni}_{0.1}\text{Fe}_{0.9}\text{S}_2$ exhibit similar structures, electronic structures and trends of OER activities to those of nanosheet powder (ESI Fig. S6†). Fig. 4a–d show the evolution of the large-scale morphology (SEM) and atomic structures (TEM) for the NiS_2 and $\text{Fe}_{0.1}\text{Ni}_{0.9}\text{S}_2$ catalysts after 5 and 50 cycles of OER measurements. The morphology of NiS_2 (Fig. 4a) is dramatically changed after 5 cycles, whilst $\text{Fe}_{0.1}\text{Ni}_{0.9}\text{S}_2$ maintains its sheet-like morphology even after 50 cycles (Fig. 4b). Furthermore, TEM images (Fig. 4c) show that most of the crystalline NiS_2 transforms into an amorphous phase after 5 cycles, whilst for $\text{Fe}_{0.1}\text{Ni}_{0.9}\text{S}_2$ only a few nm thick amorphous phase forms in the surface region (Fig. 4d) and the inner core still retains a crystalline structure. Furthermore, the phase transformation is also correlated with OER performance. As

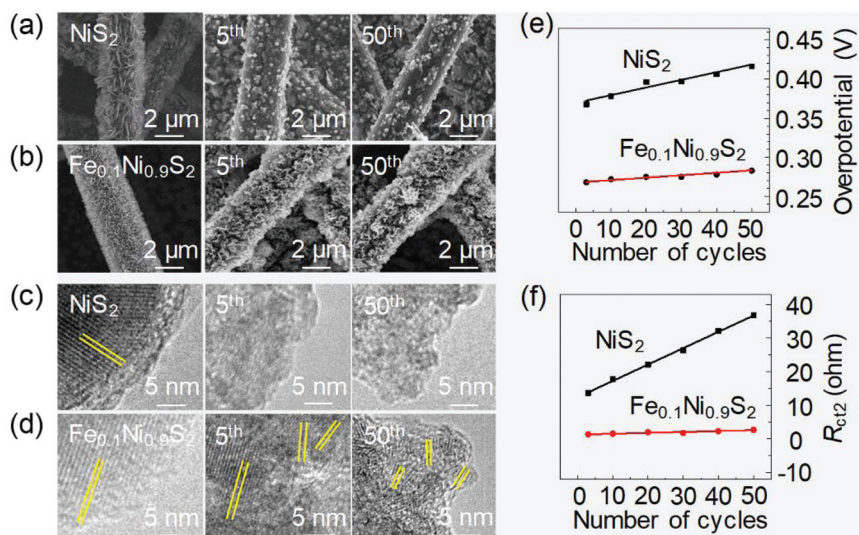


Fig. 4 (a) SEM images of the as-synthesized NiS₂ and NiS₂ after 5 and 50 cycles of OER measurements; (b) SEM images of the as-synthesized Fe_{0.1}Ni_{0.9}S₂ and Fe_{0.1}Ni_{0.9}S₂ after 5 and 50 cycles of OER measurements; (c) HRTEM images of the as-synthesized NiS₂ and NiS₂ after 5 and 50 cycles of OER measurements; (d) HRTEM images of the as-synthesized Fe_{0.1}Ni_{0.9}S₂ and Fe_{0.1}Ni_{0.9}S₂ after 5 and 50 cycles of OER measurements; (e) change of the overpotential for driving 10 mA cm⁻² current density, and (f) resistance resulting from the transformed (oxy)hydroxide layer (R_{ct2}) as a function of cycles of OER measurements.

shown in Fig. 4e, the overpotential to drive 10 mA cm⁻² current density for NiS₂ increases much faster than that for Fe_{0.1}Ni_{0.9}S₂, indicating that Ni_{0.1}Fe_{0.9}S₂ possesses better stability and activity than NiS₂. In order to understand the relationship between stability and the reconstruction process, EIS spectra after different cycles of OER measurements were collected and fitted by using an equivalent circuit model shown in Fig. 3c and Fig. S7.† R_{ct2} refers to the resistance resulting from the transformed Fe_xNi_{1-x}OOH layer and is proportional to its thickness. Fig. 4f plots the change of R_{ct2} with different cycles of OER measurements. It can be seen that the R_{ct2} for NiS₂ increases much faster than that for Fe_{0.1}Ni_{0.9}S₂, suggesting that the transformation rate for NiS₂ is faster than that for Fe_{0.1}Ni_{0.9}S₂, which corresponds to the XRD patterns of catalysts after the V-t test (Fig. S8†). These results confirm that Fe doping enhances the phase stability of NiS₂ and retards the phase transformation process.

Detailed XPS measurements were also performed to track the evolution of compositions and chemical states of the catalysts. The probe depth of XPS is around 2–4 nm.⁵³ As shown in Fig. 5a and b, the intensity of the S 2p peak substantially decreases after the OER, while a slight shift of O 1s to lower BEs with increasing OER measurements is observed because of the transformation from adsorbed oxygen to lattice oxygen (Ni-OH or Fe-OH),⁵⁴ suggesting the transformation of metal sulfides into Ni_xFe_{1-x}OOH species. For the first 5 cycles, the O 1s (Fig. 5b) and Ni 2p (Fig. 5c) spectra are in the stage of intermediate chemical states. After 50 cycles, the O 1s and Ni 2p spectra maintain similar line shapes and BEs until 200 cycles. The Ni 2p_{3/2} peak (Fig. 5c) after the OER was shifted from 853.5 eV to a higher BE of 855.1 eV, corresponding to the BE of Ni_xFe_{1-x}OOH.⁵⁵ Similar OER-induced oxidation has been observed in other Ni-based electrocatalysts.^{44,56} Interestingly, as shown in Fig. S9,† a certain amount of S is still observed on

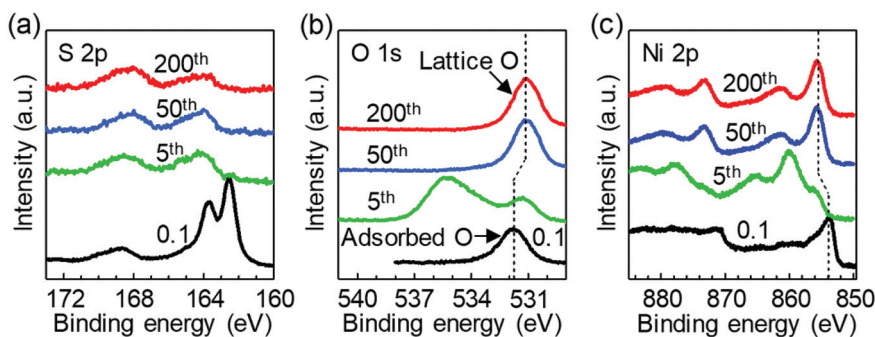


Fig. 5 XPS core levels spectra of (a) S 2p, (b) O 1s and (c) Ni 2p for the as-synthesized Fe_{0.1}Ni_{0.9}S₂ and Ni 2p for Fe_{0.1}Ni_{0.9}S₂ after 5, 50, and 200 cycles of OER measurements.

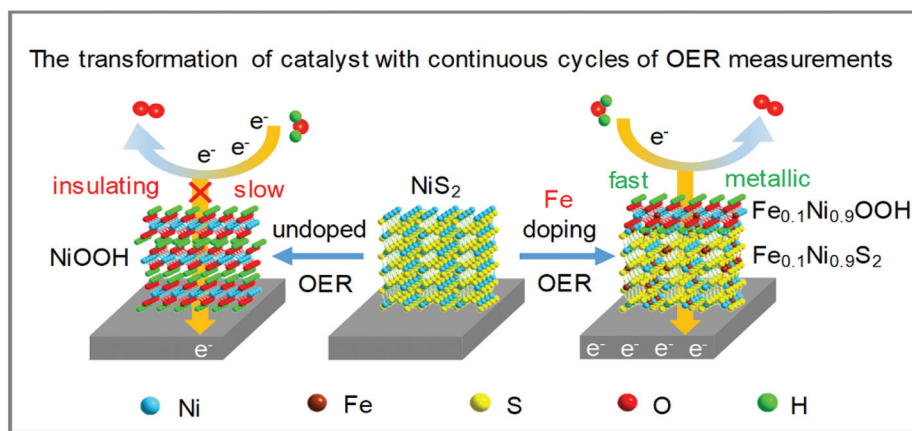


Fig. 6 Schematic illustration for phase transformation and OER activity. The NiS₂ nanosheets (left panel) completely transform into NiOOH at the beginning of a few cycles of OER measurements. The insulating NiOOH limits electron transfer and hence OER activity. In contrast, Fe doping in NiS₂ (right panel) enhances the phase stability due to stronger Fe–S bonding and retards the process of transformation. The Fe_{0.1}Ni_{0.9}S₂ catalyst can maintain its own metallic phase as a conductive channel for fast electron transfer and the thin layer of Fe_{0.1}Ni_{0.9}OOH serves as an active catalytic phase for the OER.

the catalysts even after 25 hours of stability test. Recently, Niu *et al.* reported that Se doped FeOOH lowers the energy barrier for the rate determining step from Fe–O to Fe–OOH for the OER, and thus significantly increases the OER activity.⁵⁷ It is an interesting open question whether the remaining S in NiFe (oxy)hydroxides (*i.e.*, S doped Fe_xNi_{1-x}OOH) can facilitate the reaction energetics of the OER, which has important implications for explaining the phenomenon that the transformed NiFe oxides/hydroxides from Fe_{0.1}Ni_{0.9}S₂ pre-catalysts exhibit better activity than oxides/hydroxides synthesized directly.

The above detailed characterization clearly demonstrates that the Fe_xNi_{1-x}S₂ pre-catalysts gradually transform into Fe_xNi_{1-x}OOH as the actual active species for the OER, and the Fe_{0.1}Ni_{0.9}S₂ pre-catalysts have much higher OER activity and better stability than NiS₂. We propose two possible reasons for this improvement. Firstly, the real catalyst is the transformed Ni–Fe (oxy)hydroxides. It has been established that Fe doping in Ni (oxy)hydroxides significantly improves the OER activity, with 5–10% Fe showing the highest. Secondly, the Fe_{0.1}Ni_{0.9}S₂ has better phase stability against being transformed into Fe_{0.1}Ni_{0.9}OOH. The better phase stability of Fe doped NiS₂ is attributed to a shorter Fe–S bond length of 2.259 Å in comparison with the 2.4 Å for Ni–S (details in Table S2†).^{58,59} The shorter Ni/Fe–S bond lengths suggest larger binding energies and higher energy barriers to break bonds for phase transformation. We speculate that the formation of a surface layer of Fe_xNi_{1-x}OOH as an active OER catalyst (but insulating⁴⁶) and the remaining Fe_{0.1}Ni_{0.9}S₂ as a conductive core to enable fast electron transfer is the base for the high OER activity of Fe_xNi_{1-x}S₂. As illustrated by the schematic diagram in Fig. 6, NiS₂ nanosheets quickly transform into NiOOH during the first few cycles of OER measurements, and the insulating NiOOH phase limits the electron transfer for the OER. On the other hand, Fe doping in NiS₂ enhances the phase stability of NiS₂ and retards the process of transformation due to stronger

Fe–S bonding. The thin layer of Fe_{0.1}Ni_{0.9}OOH serves as an active catalytic center for the OER and the remaining Fe_{0.1}Ni_{0.9}S₂ as a conductive channel for fast electron transfer. More generally, our results imply an important principle for design of a highly active TM chalcogenide OER catalyst, a material with structural flexibility to form a surface layer of active (oxy)hydroxides while having good stability to retain the original structure for electron conduction.

4. Conclusions

In summary, we have investigated the effect of Fe doping on the electronic structure, OER activity, and phase reconstruction process of pyrite NiS₂. Fe doping introduces more density of states at the top of the valence band and therefore increases the electronic conductivity. We identified that the Fe_{0.1}Ni_{0.9}S₂ exhibits the highest OER activity with an overpotential of 260 mV at 10 mA cm⁻² in 1 M KOH solution. We performed detailed characterization of the evolution of the structure, morphology and chemical states of the catalysts after different cycles of OER measurements. Our results further confirmed that the Fe_xNi_{1-x}S₂ pre-catalysts gradually transform into Fe_xNi_{1-x}OOH during the OER. The Fe_xNi_{1-x}OOH is the actual active species for the OER. Interestingly, we found that Fe doping retards the process of transformation because of stronger Fe–S bonding, explaining the much better electrochemical stability of Fe_{0.1}Ni_{0.9}S₂. These results suggest that the formation of a surface layer of Fe_xNi_{1-x}OOH as an active OER catalyst and the remaining Fe_{0.1}Ni_{0.9}S₂ as a conductive core to enable fast electron transfer is the base for the high OER activity of Fe_xNi_{1-x}S₂. Our work offers an important insight into metal–chalcogenide electrocatalysts for understanding the real active phase for the OER and the principle for design of highly active catalysts.

Conflicts of interest

There are no conflicts to declare.

Acknowledgements

K. H. L. Z. gratefully acknowledges financial support by the National Natural Science Foundation of China (Grant No. 21872116). D. Qi acknowledges the support of the Australian Research Council (Grant No. FT160100207). Part of this research was undertaken on the Soft X-ray Spectroscopy beamline at the Australian Synchrotron, part of ANSTO. We acknowledge the support from beamline scientist Dr Bruce Cowie at the Australian Synchrotron.

Notes and references

- X. Zou and Y. Zhang, *Chem. Soc. Rev.*, 2015, **44**, 5148–5180.
- B. Wurster, D. Grumelli, D. Hoetger, R. Gutzler and K. Kern, *J. Am. Chem. Soc.*, 2016, **138**, 3623–3626.
- M. S. Burke, L. J. Enman, A. S. Batchellor, S. Zou and S. W. Boettcher, *Chem. Mater.*, 2015, **27**, 7549–7558.
- H. B. Tao, L. Fang, J. Chen, H. B. Yang, J. Gao, J. Miao, S. Chen and B. Liu, *J. Am. Chem. Soc.*, 2016, **138**, 9978–9985.
- Y. Ji, L. Yang, X. Ren, G. Cui, X. Xiong and X. Sun, *ACS Sustainable Chem. Eng.*, 2018, **6**, 9555–9559.
- J. Zhao, X. Li, G. Cui and X. Sun, *Chem. Commun.*, 2018, **54**, 5462–5465.
- C. Ouyang, X. Wang, C. Wang, X. Zhang, J. Wu, Z. Ma, S. Dou and S. Wang, *Electrochim. Acta*, 2015, **174**, 297–301.
- C. Guan, X. Liu, A. M. Elshahawy, H. Zhang, H. Wu, S. J. Pennycook and J. Wang, *Nanoscale Horiz.*, 2017, **2**, 342–348.
- P. Chen, K. Xu, Z. Fang, Y. Tong, J. Wu, X. Lu, X. Peng, H. Ding, C. Wu and Y. Xie, *Angew. Chem., Int. Ed.*, 2015, **54**, 14710–14714.
- Y. Zhang, B. Ouyang, J. Xu, G. Jia, S. Chen, R. S. Rawat and H. J. Fan, *Angew. Chem., Int. Ed.*, 2016, **55**, 8670–8674.
- M. Liu and J. Li, *ACS Appl. Mater. Interfaces*, 2016, **8**, 2158–2165.
- X.-Y. Yu, Y. Feng, B. Guan, X. W. Lou and U. Paik, *Energy Environ. Sci.*, 2016, **9**, 1246–1250.
- B. Hammer and J. K. Nørskov, *Adv. Catal.*, 2000, **45**, 71–129.
- J. Suntivich, K. J. May, H. A. Gasteiger, J. B. Goodenough and Y. Shao-Horn, *Science*, 2011, **334**, 1383.
- W. T. Hong, K. A. Stoerzinger, Y.-L. Lee, L. Giordano, A. Grimaud, A. M. Johnson, J. Hwang, E. J. Crumlin, W. Yang and Y. Shao-Horn, *Energy Environ. Sci.*, 2017, **10**, 2190–2200.
- A. Grimaud, K. J. May, C. E. Carlton, Y.-L. Lee, M. Risch, W. T. Hong, J. Zhou and Y. Shao-Horn, *Nat. Commun.*, 2013, **4**, 2439.
- A. Grimaud, O. Diaz-Morales, B. Han, W. T. Hong, Y.-L. Lee, L. Giordano, K. A. Stoerzinger, M. T. M. Koper and Y. Shao-Horn, *Nat. Chem.*, 2017, **9**, 457–465.
- X. Cheng, E. Fabbri, M. Nachtegaal, I. E. Castelli, M. El Kazzi, R. Haumont, N. Marzari and T. J. Schmidt, *Chem. Mater.*, 2015, **27**, 7662–7672.
- C. Wei, Z. Feng, M. Baisariyev, L. Yu, L. Zeng, T. Wu, H. Zhao, Y. Huang, M. J. Bedzyk, T. Sritharan and Z. J. Xu, *Chem. Mater.*, 2016, **28**, 4129–4133.
- M. Al-Mamun, Z. Zhu, H. Yin, X. Su, H. Zhang, P. Liu, H. Yang, D. Wang, Z. Tang, Y. Wang and H. Zhao, *Chem. Commun.*, 2016, **52**, 9450–9453.
- G. Fu, X. Wen, S. Xi, Z. Chen, W. Li, J.-Y. Zhang, A. Tadich, R. Wu, D.-C. Qi, Y. Du, J. Cheng and K. H. L. Zhang, *Chem. Mater.*, 2019, **31**, 419–428.
- J. R. Petrie, V. R. Cooper, J. W. Freeland, T. L. Meyer, Z. Zhang, D. A. Lutterman and H. N. Lee, *J. Am. Chem. Soc.*, 2016, **138**, 2488–2491.
- K. A. Stoerzinger, W. S. Choi, H. Jeon, H. N. Lee and Y. Shao-Horn, *J. Phys. Chem. Lett.*, 2015, **6**, 487–492.
- Y. Tong, Y. Guo, P. Chen, H. Liu, M. Zhang, L. Zhang, W. Yan, W. Chu, C. Wu and Y. Xie, *Chem*, 2017, **3**, 812–821.
- T. Zhang, M.-Y. Wu, D.-Y. Yan, J. Mao, H. Liu, W.-B. Hu, X.-W. Du, T. Ling and S.-Z. Qiao, *Nano Energy*, 2018, **43**, 103–109.
- Z. Wang, X. Ren, L. Wang, G. Cui, H. Wang and X. Sun, *Chem. Commun.*, 2018, **54**, 10993–10996.
- J. Wang, W. Cui, Q. Liu, Z. Xing, A. M. Asiri and X. Sun, *Adv. Mater.*, 2016, **28**, 215–230.
- K. Xu, P. Chen, X. Li, Y. Tong, H. Ding, X. Wu, W. Chu, Z. Peng, C. Wu and Y. Xie, *J. Am. Chem. Soc.*, 2015, **137**, 4119–4125.
- A. T. Swesi, J. Masud and M. Nath, *Energy Environ. Sci.*, 2016, **9**, 1771–1782.
- L.-A. Stern, L. Feng, F. Song and X. Hu, *Energy Environ. Sci.*, 2015, **8**, 2347–2351.
- W. Zhou, X.-J. Wu, X. Cao, X. Huang, C. Tan, J. Tian, H. Liu, J. Wang and H. Zhang, *Energy Environ. Sci.*, 2013, **6**, 2921–2924.
- K. H. L. Zhang, K. Xi, M. G. Blamire and R. G. Egdell, *J. Phys.: Condens. Matter*, 2016, **28**, 19.
- A. Kuc, T. Heine and A. Kis, *MRS Bull.*, 2015, **40**, 577–584.
- A. Fujimori, K. Mamiya, T. Mizokawa, T. Miyadai, T. Sekiguchi, H. Takahashi, N. Mōri and S. Suga, *Phys. Rev. B: Condens. Matter Mater. Phys.*, 1996, **54**, 16329–16332.
- Q. Ma, C. Hu, K. Liu, S.-F. Hung, D. Ou, H. M. Chen, G. Fu and N. Zheng, *Nano Energy*, 2017, **41**, 148–153.
- X. Zheng, X. Han, Y. Zhang, J. Wang, C. Zhong, Y. Deng and W. Hu, *Nanoscale*, 2019, **11**, 5646–5654.
- H. Liu, Q. He, H. Jiang, Y. Lin, Y. Zhang, M. Habib, S. Chen and L. Song, *ACS Nano*, 2017, **11**, 11574–11583.
- J. Yan, H. Wu, L. Ping, H. Chen, R. Jiang and S. Liu, *J. Mater. Chem. A*, 2017, **5**, 10173–10181.
- X. Long, Z. Ma, H. Yu, X. Gao, X. Pan, X. Chen, S. Yang and Z. Yi, *J. Mater. Chem. A*, 2016, **4**, 14939–14943.

- 40 G. Zhang, Y.-S. Feng, W.-T. Lu, D. He, C.-Y. Wang, Y.-K. Li, X.-Y. Wang and F.-F. Cao, *ACS Catal.*, 2018, **8**, 5431–5441.
- 41 C. Tang, A. M. Asiri and X. Sun, *Chem. Commun.*, 2016, **52**, 4529–4532.
- 42 J. Zhuo, M. Caban-Acevedo, H. Liang, L. Samad, Q. Ding, Y. Fu, M. Li and S. Jin, *ACS Catal.*, 2015, **5**, 6355–6361.
- 43 S. Jin, *ACS Energy Lett.*, 2017, **2**, 1937–1938.
- 44 B. R. Wygant, K. Kawashima and C. B. Mullins, *ACS Energy Lett.*, 2018, **3**, 2956–2966.
- 45 C. Tang, N. Cheng, Z. Pu, W. Xing and X. Sun, *Angew. Chem., Int. Ed.*, 2015, **54**, 9351–9355.
- 46 L. Trotochaud, S. L. Young, J. K. Ranney and S. W. Boettcher, *J. Am. Chem. Soc.*, 2014, **136**, 6744–6753.
- 47 N. Elliott, *J. Chem. Phys.*, 1960, **33**, 903–905.
- 48 J. M. Honig and J. Spalek, *Chem. Mater.*, 1998, **10**, 2910–2929.
- 49 S. R. Krishnakumar and D. D. Sarma, *Phys. Rev. B: Condens. Matter Mater. Phys.*, 2003, **68**, 155110.
- 50 J. F. W. Mosselmans, R. A. D. Pattick, G. van der Laan, J. M. Charnock, D. J. Vaughan, C. M. B. Henderson and C. D. Garner, *Phys. Chem. Miner.*, 1995, **22**, 311–317.
- 51 Q. Li, D. Wang, C. Han, X. Ma, Q. Lu, Z. Xing and X. Yang, *J. Mater. Chem. A*, 2018, **6**, 8233–8237.
- 52 S. Klaus, Y. Cai, M. W. Louie, L. Trotochaud and A. T. Bell, *J. Phys. Chem. C*, 2015, **119**, 7243–7254.
- 53 K. H. L. Zhang, D. J. Payne, R. G. Palgrave, V. K. Lazarov, W. Chen, A. T. S. Wee, C. F. McConville, P. D. C. King, T. D. Veal, G. Panaccione, P. Lacovig and R. G. Egdell, *Chem. Mater.*, 2009, **21**, 4353–4355.
- 54 X. Xu, F. Song and X. Hu, *Nat. Commun.*, 2016, **7**, 12324.
- 55 B. Konkena, J. Masa, A. J. R. Botz, I. Sinev, W. Xia, J. Koßmann, R. Drautz, M. Muhler and W. Schuhmann, *ACS Catal.*, 2017, **7**, 229–237.
- 56 K. Xu, H. Cheng, L. Liu, H. Lv, X. Wu, C. Wu and Y. Xie, *Nano Lett.*, 2017, **17**, 578–583.
- 57 S. Niu, W.-J. Jiang, Z. Wei, T. Tang, J. Ma, J.-S. Hu and L.-J. Wan, *J. Am. Chem. Soc.*, 2019, **141**, 7005–7013.
- 58 C. Yu, H. Huang, S. Zhou, X. Han, C. Zhao, J. Yang, S. Li, W. Guo, B. An, J. Zhao and J. Qiu, *Nano Res.*, 2018, **11**, 3411–3418.
- 59 M. Elliott, *J. Chem. Phys.*, 1960, **33**, 903–905.